applied sciences

IMPACT FACTOR 2.5

CITESCORE 5.3

Article

Analysis of Beam Walk in Inter-Satellite Laser Link: Implications for Differential Wavefront Sensing in Gravitational Wave Detection

Xing-Guang Qian, Zhao Cui, Hao-Qi Shi, Xue Wang, Wei-Lai Yao, Rui-Hong Gao and Yi-Kun Wang

Special Issue

Advances in Optical Instrument and Measurement Technology

Edited by

Prof. Dr. Zhan Gao, Dr. Jiakun Li and Dr. Qixin He

MDPI

https://doi.org/10.3390/app14135526

applied sciences

MDPI

Article

Analysis of Beam Walk in Inter-Satellite Laser Link: Implications for Differential Wavefront Sensing in Gravitational Wave Detection

Xing-Guang Qian [1,2], Zhao Cui [1,2,3], Hao-Qi Shi [1,2], Xue Wang [1,2,3], Wei-Lai Yao [1,2,3], Rui-Hong Gao [4,*] and Yi-Kun Wang [1,2,*]

[1] School of Physics and Photoelectric Engineering, Key Laboratory of Gravitational Wave Precision Measurement of Zhejiang Province, Taiji Laboratory for Gravitational Wave Universe, Hangzhou Institute for Advanced Study, University of Chinese Academy of Sciences, Hangzhou 310024, China; qianxingguang21@mails.ucas.ac.cn (X.-G.Q.); cz447047276@163.com (Z.C.); shihaoqi22@mails.ucas.ac.cn (H.-Q.S.); wangxue1998115@163.com (X.W.); yaoweilai18@mails.ucas.ac.cn (W.-L.Y.)

[2] University of Chinese Academy of Sciences, Beijing 101408, China

[3] Shanghai Institute of Technical Physics, Chinese Academy of Sciences, Shanghai 200031, China

[4] Center for Gravitational Wave Experiment, National Microgravity Laboratory, Institute of Mechanics, Chinese Academy of Sciences, Beijing 100190, China

* Correspondence: gaoruihong@imech.ac.cn (R.-H.G.); wangyikun@ucas.ac.cn (Y.-K.W.)

Abstract: Achieving space-based gravitational wave detection requires the establishment of an interferometer constellation. It is necessary to establish and maintain stable laser interferometric links using the differential wavefront sensing (DWS) technnique. When the distant measurement beam experiences pointing jitter, it causes beam walk on the surface of the local detector. The reduced overlap between the local reference spot and the distant spot increases the nonlinear errors in the DWS technique, which need to be suppressed. Numerical analysis was conducted on the spatial beam interference signals of the DWS technique when the distant measurement beam experienced pointing jitter. An experimental measurement system was designed, and the beam walk was suppressed using a conjugate imaging system. The results show that within a range of 300 μrad, the optical path with the imaging system can reduce measurement errors by at least 83%. This way also helps to reduce pointing jitter noise in inter-satellite links, thereby improving laser pointing control accuracy.This method would provide a valuable reference for future DWS measurement systems.

Keywords: beam walk; angle measurement error; differential wavefront sensing; inter-satellite laser link; laser pointing jitter

Citation: Qian, X.-G.; Cui, Z.; Shi, H.-Q.; Wang, X.; Yao, W.-L.; Gao, R.-H.; Wang, Y.-K. Analysis of Beam Walk in Inter-Satellite Laser Link: Implications for Differential Wavefront Sensing in Gravitational Wave Detection. *Appl. Sci.* **2024**, *14*, 5526. https://doi.org/10.3390/app14135526

Academic Editor: Luca Poletto

Received: 10 May 2024
Revised: 21 June 2024
Accepted: 21 June 2024
Published: 25 June 2024

1. Introduction

The LIGO scientific collaboration and the VIRGO team detected gravitational waves from the merger of two black holes on 14 September 2015 [1,2]. This marked a significant leap forward for gravitational astronomy. Ground-based gravitational wave detectors are affected by seismic noise, correlated gravity gradient noise, and thermal noise from the final stages of suspension and test masses, generally limiting their detection capabilities to high-frequency gravitational waves above 10 Hz. Space-based gravitational wave detectors are situated in an excellent vacuum environment far from Earth-based noise sources. Space-based gravitational wave detection involves constructing constellations of interferometers with extremely long arm lengths while employing drag-free spacecraft technology. By using payloads such as inertial sensors and micro-thrusters to counteract non-conservative forces, these detectors can effectively detect low-frequency gravitational waves [3]. Notable examples include the LISA (Laser Interferometer Space Antenna) mission and China's Taiji program [3,4].

Gravitational wave detection in space involves the deployment of Michelson interferometers, having arm lengths ranging from tens to millions of kilometers [5–7]. To discern gravitational wave signals, these systems measure relative distance variations at the picometer scale through heterodyne interferometry [3,8]. Differential wavefront sensing is used to establish laser interferometric links. By measuring the phase difference between the local and distal incident beams and converting it into an angle, this information is used for satellite drive control. This forms the basis for establishing and maintaining stable laser links [4,9,10]. After the satellite is launched into space, it experiences jitter due to the influence of complex space environments such as solar wind and cosmic rays, which are non-conservative forces. The drag-free control system will ensure the satellite's attitude stability as much as possible [11]. However, residual errors will still couple into the outgoing laser. The telescope on the receiving satellite platform will amplify this jitter. Ultimately, this jitter will couple into the image plane of the Quadrant Photodiode (QPD) detector, causing beam walk of the distal incident measurement beam on the image plane. The overlap between the distal instant measurement beam and the local beam will be reduced, affecting the measurement results of the DWS technique. As illustrated in Figure 1a, pointing jitter leads to variations in the angle between the incident and local beam, manifesting as differential beam walk lengths on the QPD image plane.The measurement performance of the DWS technique in this situation is shown in Figure 1b. Measurement errors caused by beam walk may affect the results of measuring the angle between the distant beam and the local beam. The angle between the two beams serves as a direct feedback parameter for satellite link establishment. If there is a significant deviation between the DWS measured angle and the actual angle, it could impact both the establishment and stability of the link. This could potentially lead to the failure of gravitational wave detection [12–14]. Consequently, it is crucial to explore the correlation between beam walk and the DWS signal.

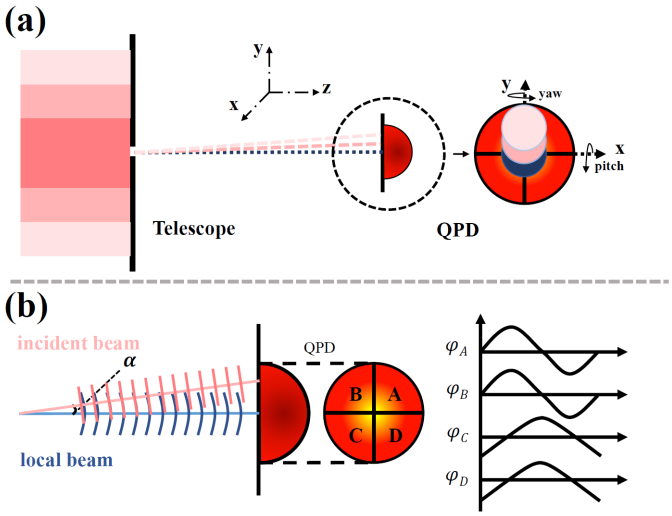

Figure 1. (**a**) Coincidingwiththe local beam, the distal incident beam is incident vertically to the center of QPD without beam walk. When beam walk exists in the pitch direction, the spot will shift in the y-axis direction. (**b**) The measurement results of the DWS technique when beam walk occurs in the incident beam. The left side indicates the interference conditions, while the right side shows the phases of each quadrant.

Studies have been conducted on the technical characteristics of DWS and beam walk. Previous research by Duan et al. [15] introduced an analytical model for the DWS technique centered on Gaussian beam propagation, emphasizing the significant nonlinear effects in DWS signals, which necessitate consideration during the system's design and calibration. In the context of the LISA program, Chwalla et al. [12] in 2012 proposed employing a pupil relay imaging system to curtail beam walk arising from measurement beam pointing jitter. In 2018, Tröbs et al. [16] devised an imaging system featuring a tiltable beam in

the test mass interferometer, achieving minimized beam walk by adjusting the lens pitch. Meshksar et al. [17] in 2021 posited that enhancing the detection range of the differential power sensing (DPS) signal is feasible by incorporating a lens to mitigate beam walk within a dual Gaussian beam interference framework. GAO et al. [18,19] analyzed the linear performance of the DWS technique in the case of Gaussian beam–Gaussian flat-top beam interference, as well as the impact of DWS on the static pointing error of gravitational wave detection satellites and proposed a zero-offset reduction scheme. A technique for enhancing the sensitivity of the torsion pendulum system by employing the DWS optical readout was proposed by Wang et al. [20], and the results indicated that the angular resolution of the DWS signal in optical readout mode can reach the level of 10 nrad/$Hz^{1/2}$ over the full measurement band. Qi et al. [21] derived from the theoretical model of the DWS method that increasing the wavefront curvature of the measured laser beam can significantly improve the sensitivity to lateral displacement. Hao Yan [22] built a quasi-monolithic compact interferometer bench for dihedral-angle error measurement and test by the DWS technique. The experimental results showed that a resolution of ±0.15 μrad and a nonlinear residual below ±3 μrad within a dynamic range of ±100 μrad was achieved.

Few researchers have delved into the ramifications of beam walk on the DWS signal. In this work, the correlation between beam walk and DWS signals resulting from the interference of Gaussian and Gaussian flat-top beams was scrutinized via physical modeling and numerical simulation. Then, a conjugate imaging system was constructed using two plano-convex lenses to verify the effectiveness of suppressing beam walk through conjugate position imaging. Finally, a simulation experimental platform for the DWS measurement process was set up. By introducing perturbations to the distant measurement beam, the effectiveness of the imaging system in suppressing nonlinear errors caused by the beam walk was validated.

The structure of this paper is delineated in the following manner: Section 2 establishes a physical model of the DWS signal, interfered by Gaussian and Gaussian flat-top beams, and delves into the linear characteristics of the DWS signal in light of the Gaussian flat-top beam walk using numerical simulations. Section 3 presents the design and creation of an inter-satellite laser link simulation system, accompanied by an experimental setup designed to rectify the beam walk through an imaging system. In Section 4, measurements of the DWS angle are taken across different lengths of beam walk, comparing outcomes with and without the imaging system. Conclusions are subsequently drawn based on the synthesis of these simulations and experimental insights.

2. Analysis of the Relationship between Beam Walk and DWS Signal

2.1. DWS Interference Signal Model in Practical Situation

As deduced from the prior discussions, the DWS signal undergoes interference from both the local Gaussian beam and the distant Gaussian flat-top beam [15,18]. Utilizing a rectangular spatial coordinate with the laser source at the origin, the primary mode of Gaussian beam propagating along the z-axis can be represented as follows:

$$E_{G(x,y,z)} = \frac{A_0}{\omega(z_g)} \cdot e^{-\frac{x^2+y^2}{\omega^2(z_g)} - ik\left[\frac{x^2+y^2}{2R(z_g)} + i\phi(z_g) + z_g\right]} \quad (1)$$

where A_0 is the laser power factor, z_g is the propagation distance of the Gaussian beam, $\omega(z_g)$ and $R(z_g)$ represents the spot radius and radius of the wavefront curvature at z_g position, respectively, and $\phi(z_g)$ is the additional phase shift.

The laser emitted from the distal satellite platform will diffuse after far-field transmission, resulting in a spot size much larger than the aperture of the local satellite platform telescope. Therefore, the laser entering the telescope can be approximated as a parallel beam [18]. Within the same rectangular spatial coordinate system, anchored at the laser source, the complex amplitude of the flat-top beam propagating along the z-axis can be succinctly represented as follows:

$$E_{ft(x,y,z)} = E_0 e^{-ikz_f} @ (x^2 + y^2 \leq {\omega_f}^2) \tag{2}$$

where E_0 is the amplitude, ω_f is the radius of the flat-top beam spot on the QPD surface, and z_f is the propagation distance of the flat-top beam.

In the actual case, the distal incident beam's Gaussian flat-top profile gets truncated by the circular aperture of the receiving telescope, illustrated by the dotted blue circle in Figure 2a. Given the marginal intensity of the interferometric signal in the peripheral integration zone, this study simplifies the analysis by assuming that the Gaussian flat-top beam is truncated by a square aperture, represented by the blue box in Figure 2b. This approximation does not significantly alter the qualitative analysis.

This study primarily examines the beam walk in the x-axis direction to understand its relationship with the DWS signal, though conclusions drawn are equally applicable to the pitch direction.

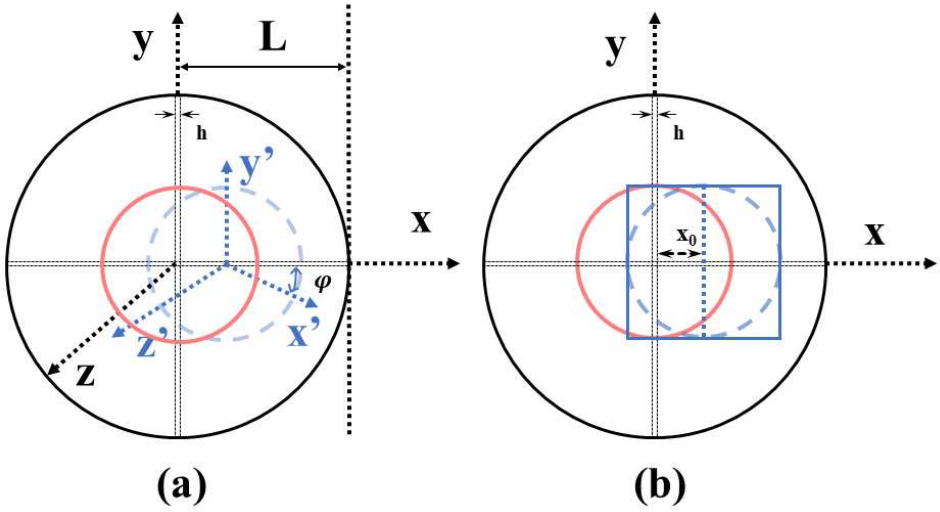

Figure 2. Representation of interference dynamics amidst x-axis beam walk. (**a**) Depicts the QPD surface within the black circle. The centrally injected local Gaussian beam is denoted by the red circle, while the blue circle with the dotted line demonstrates the beam walk of the distant Gaussian flat-top spot, establishing an angle φ between the two beams. (**b**) Exhibits Gaussian flat-top beam post-square-aperture truncation, encapsulated in the blue box. Here, the y-axis integration ranges for both left and right quadrants extend from $-\omega_f$ to ω_f, whereas the x-axis spans from $(x_0 - \frac{\omega_f}{\cos(\varphi)}, -h)$ to $(h, x_0 + \frac{\omega_f}{\cos(\varphi)})$.

The interferometric signal's complex amplitude within the left semi-quadrant can be expressed as follows:

$$F_{left} = \int s_{left} dS \cdot E_{G(x,y,z)} E_{ft(x,y,z)} \tag{3}$$

The complex amplitude for the interferometric signal in the right semi-quadrant is given by the following:

$$F_{right} = \int s_{left} dS \cdot E_{G(x,y,z)} E_{ft(x,y,z)} \tag{4}$$

The preceding two integral expressions can be succinctly denoted as follows:

$$F_{left} = E_0 \cdot B_1 \cdot B_2 \cdot B_3 \tag{5}$$

$$F_{right} = E_0 \cdot B_1 \cdot B_2 \cdot B_4 \tag{6}$$

where B_1, B_2, B_3, and B_4 can be determined as follows:

$$B_1 = \frac{A_0}{\omega(z_g)} \cdot e^{[-i\varphi(z_g) - ikz_g - ik\sin(\phi)x_0 + ikz_f]} \tag{7}$$

$$B_2 = \int_{-w_f}^{w_f} e^{-\frac{y^2}{\omega^2(z_g)} - \frac{iky^2}{2R(z_g)}} dy \tag{8}$$

$$B_3 = \int_{x_0 - \frac{\omega_f}{\cos(\varphi)}}^{-h} e^{-\frac{x^2}{\omega^2(z_g)} - \frac{ikx^2}{2R(z_g)} + ik\sin(\varphi)x} dx \tag{9}$$

$$B_4 = \int_{h}^{x_0 + \frac{\omega_f}{\cos(\varphi)}} e^{-\frac{x^2}{\omega^2(z_g)} - \frac{ikx^2}{2R(z_g)} + ik\sin(\varphi)x} dx \tag{10}$$

The DWS signal is shown as follows:

$$DWS = \arg(F_{right}) - \arg(F_{left}) \tag{11}$$

From the provided equation, the DWS signal prominently hinges on the beam angle φ, QPD quadrant gap h, the spot size ω_f, and the Gaussian flat-top spot offset x_0 on the QPD detection surface. Conversely, the detector size L bears no relevance to the analysis.

2.2. Numerical Simulation Analysis of Beam Walk

The phenomenon of beam walk, associated with the Gaussian flat-top beam, alters the region of spot overlap on the QPD detection surface, consequently impacting the integration area for the DWS signal. In the numerical simulation, the radius of the QPD detector's image plane L is set to 1 mm with the gap h of 25 µm. The laser wavelength is 1064 nm. The radius of the Gaussian spot and the Gaussian flat-top spot are 0.5 mm. The propagation distance of the Gaussian beam is 0.5 m with a power of 20 mW. The power of the Gaussian flat-top beam is 100 pW.

With a beam walk of x_0 in the yaw direction from the distant Gaussian flat-top beam, as depicted in Figure 2b, the integration areas along the x-axis are delineated as $(x_0 - \frac{\omega_f}{\cos(\varphi)}, -h)$ and $(h, x_0 + \frac{\omega_f}{\cos(\varphi)})$. GAO [18] indicated, in the context of the Taiji program, that the angle deviation for the incident beam, relative to QPD, ranges between 300 µrad and −300 µrad. The angle measurement discrepancy attributed to the DWS methodology must not exceed 300 nrad. Hence, any area where the error remains below 300 nrad is classified as the linear region.

$$|\Delta\varphi(\varphi)| = \left| \frac{DWS(\varphi)}{k} - \varphi \right| \leq 300 \text{ nrad} \cdots \forall\varphi \in [-300 \text{ µrad}, 300 \text{ µrad}] \tag{12}$$

where φ is the angle between the two beams, $\Delta\varphi(\varphi)$ is the angular measurement error caused by the nonlinearity of the DWS technique, DWS(φ) is the measured DWS signal value, and k is the slope of the linear curve fitting. The DWS signal and angle measurement error $\Delta\varphi(\varphi)$ are illustrated in the Figure 3 without the beam walk.

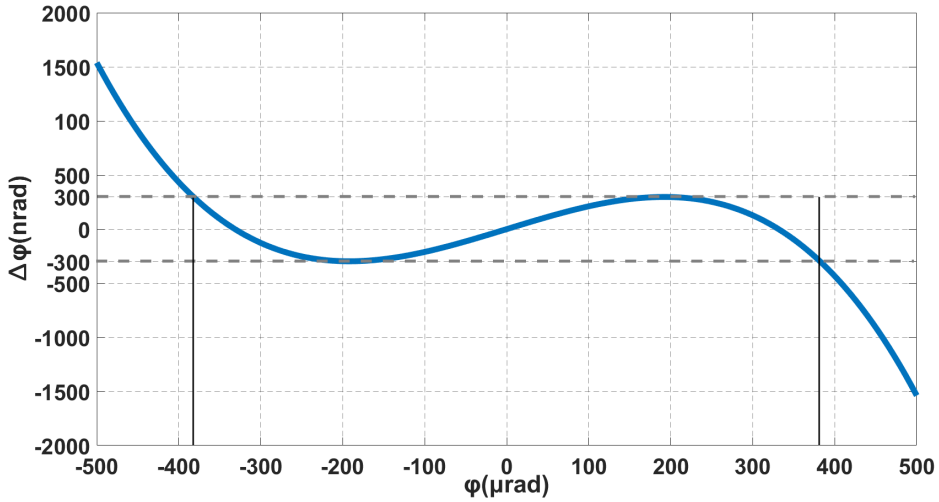

Figure 3. Variation of angle measurement error $\Delta\varphi(\varphi)$ in the absence of beam walk (0 μm Scenario).

When the measured light beam undergoes pointing jitter, it is considered to be the motion around the exit pupil of the telescope, namely the entrance pupil motion of the optical platform. Due to the extremely small angle of deflection and the fact that the optical platform only refracts the incident light beam, the beam walk caused by the image plane is approximately equal to the arc length. It can be obtained by the following formula:

$$\Delta l \approx \Delta\varphi \cdot R \tag{13}$$

Δl represents the offset of the light beam relative to the center point of the QPD, $\Delta\varphi$ denotes the angular offset, and R stands for the beam propagation distance. Given a fixed beam propagation distance, as the angular offset changes, the beam walk increases with the increasing angular offset. Assuming an axial propagation distance of 2 m, the relationship between the beam walk at different degrees and the numerical results of the DWS technique, as well as phase angle conversion results, can be established, as shown in the Figure 4.

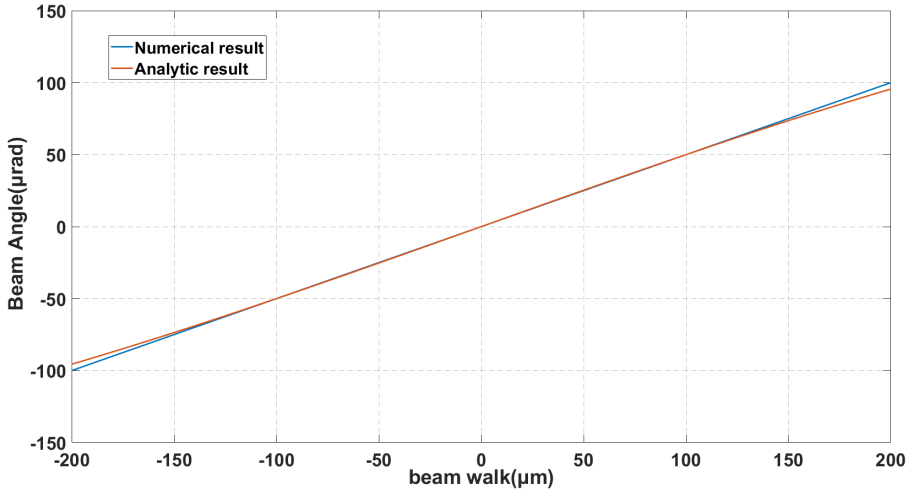

Figure 4. DWS signals for various degrees of beam walk during light propagation over a 2 m axial distance.

The angular measurement error under different beam offsets can be obtained by subtracting the numerical results of the DWS technique from the phase angle conversion results, as shown in Figure 5.

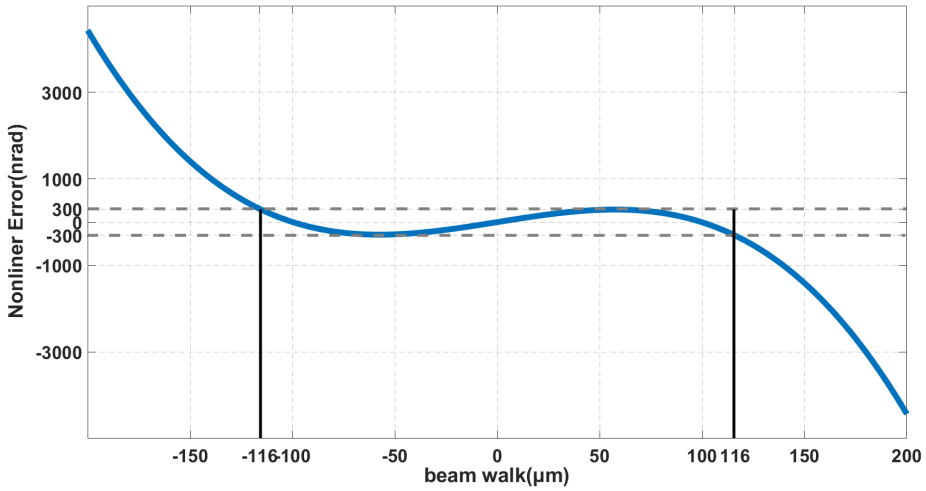

Figure 5. DWS error signals for various degrees of beam walk during light propagation over a 2 m axial distance.

It can be observed that when the beam walk is approximately within ±116 μm, it meets the requirement of angular measurement error within ±300 μrad. For the maximum beam offset, since the axial propagation distance of the beam is 2 m, the resulting beam angular deviation can be calculated to be approximately ±58 μrad using Equation (13), which is significantly below the required ±300 μrad range for DWS nonlinearity specified by the Taiji program.

As the propagation distance decreases, theoretically, the beam walk caused by the same angle will also decrease. Thus, reducing the distance may be effective in reducing measurement errors. Therefore, it is necessary to investigate when, under different propagation distances, the ±300 nrad angular measurement error boundary can be met to achieve an angular range of ±300 μrad.

Figure 6 indicates that the optimal propagation distance must not exceed 0.16 m, correlating with a beam walk of 48 μm. An increase in the beam walk expands the angle measurement range, yet the measurement error surpasses ±300 μrad, a threshold that is impermissible. To ensure a measurement range beyond ±300 μrad amid beam walk, it becomes imperative to constrain the Gaussian flat-top beam's propagation distance. Nonetheless, achieving a propagation distance under 0.16 m for the Gaussian flat-top beam poses a significant challenge in practical engineering applications. Consequently, strategies to curtail the beam walk demand serious consideration.

The angle measurement capacity of the DWS technique is inherently constrained. Figure 3 illustrates the correlation between the angle measurement error and beam angle when the beam walk equals =0 μm. The data suggest an approximate angular measurement range φ of ±400 μrad, indicating that the linear region is adequate when both beams are aligned at the QPD's center. The analysis underscores the substantial nonlinearity of the DWS signal induced by beam walk, a factor that exacerbates the angle measurement error and restricts its range. To accommodate angle measurements across varying beam propagation distances, it is essential to minimize the beam walk distance generated by the pointing jitter of the Gaussian flat-top beam on the QPD surface.

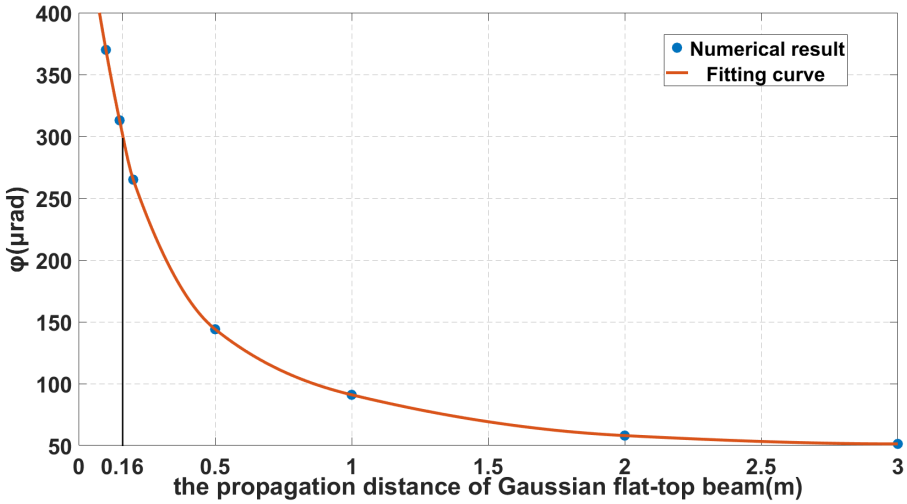

Figure 6. Correlation between propagation distance and angle measurement precision. Note: Blue dots represent the magnitude of angle measurement errors that fall within the Taiji program's acceptable linearity range across various propagation distances, while the orange line depicts the trend through linear fitting.

3. DWS Measurement Error Suppression Strategy

In the face of measurement nonlinearity induced by beam walk, adjusting the distance from the measurement beam entrance pupil to the detector enables meeting the requirements of directional measurements for the Taiji program. However, preliminary factors such as interference platform design, ground installation and adjustment, telescope, and interference measurement platform coupling render this method challenging to implement. Based on DWS measurement results without beam walk, suppressing the beam walk amount of the QPD image plane and ensuring optimal overlap of interference spots emerge as the foremost considerations for resolving this issue.

3.1. Design of Imaging System Parameters

To achieve effective correction of the beam walk while minimizing the introduction of additional sources of error, starting from geometrical optics, employing the method of conjugate imaging can ensure object–image conjugation. Theoretically, this approach can avoid introducing additional aberrations, and for ideal optical systems, it can achieve symmetrical imaging while keeping the angular characteristics of beam jitter unchanged.

As shown in Figure 7, this design utilizes two plano-convex lenses arranged in parallel with a separation of twice the focal length. The exit pupil and entrance pupil are positioned at the focal points of the front and rear lenses of the imaging system, respectively.

In actual experiments, we employed the LA1433-C plano-convex lens (Thorlabs, Newton, NJ, USA) produced by Thorlabs, with a size of 1 inch and front and rear focal lengths of 149.5 mm and 147.5 mm, respectively. The anti-reflection coating wavelength range is 1050–1700 nm, making it effective for the subsequent experiments utilizing a 1064 nm laser.

Simultaneously, we utilized a combination design of high-precision telescoping sleeves and clamp wrenches to ensure precise positioning of the optical elements. The telescoping sleeve allows for a travel range of 4 mm, with high-precision control of 0.5 mm per rotation, and prevents rotation of the optical elements during movement. During the optical path alignment process, it is consistently required to orient the convex surface towards the direction of beam incidence, as refraction through both surfaces ensures the outgoing beam achieves optimal focusing.

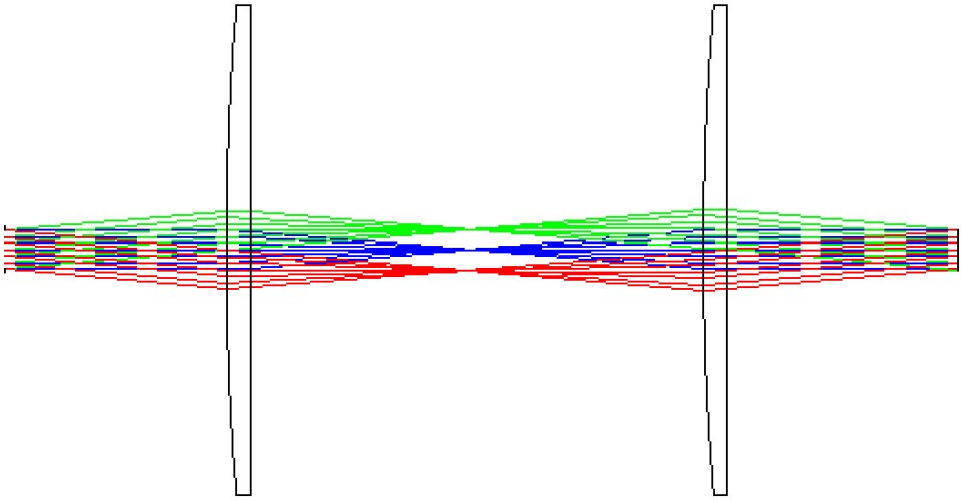

Figure 7. Design of imaging system.

3.2. Design Results of the Imaging System

The corrective efficacy of the imaging system for angular deviations was validated using a Gaussian beam with variable angles in Zemax. This process entailed measuring the centroid coordinates of the beam at the exit pupil under different angular shifts. As delineated in Table 1, the Gaussian beams were adjusted by 0.1 mrad, 0.2 mrad, 0.5 mrad, and 0.8 mrad, respectively. The resulting centroid coordinate offsets were all under 1 µm, and there was no significant alteration in the spot radius. These observations affirm that the imaging system can proficiently rectify the beam walk without inducing spot distortion.

Table 1. Simulation results with an angular offset in x axis.

Offset/mrad	Center of X/mm	Center of Y/mm	x-Axis Radius/mm	y-Axis Radius/mm
0	−0.00005638	−0.00006197	0.24985080	0.25016640
0.1	−0.00007094	−0.00006395	0.24985112	0.25009686
0.2	−0.00009681	−0.00013026	0.24986038	0.25001645
0.5	−0.00032305	−0.00013623	0.24988321	0.24992484
0.8	−0.00053520	−0.00000460	0.24996465	0.25003379

4. Inter-Satellite Link Angle Measurement Simulation Experiment

From the above analysis, it can be concluded that the beam walk affects the results of the DWS measurements, leading to unnecessary nonlinear errors. Meanwhile, the design employing dual-lens conjugate imaging effectively suppresses the beam walk. To validate the feasibility of this approach in practical usage, an inter-satellite link pointing control system was constructed. Angle measurement data were obtained both with and without the addition of the imaging system, followed by thorough analysis.

4.1. Design of Pointing Angle Measurement System

In 2022, GAO et al. [19] proposed that zero-offset analysis on the DWS technique would affect the absolute angle measurement error and designed an experimental system to verify the hypothesis. The zero-offset is theoretically eliminated at the beam waist position. To reduce the impact of zero-offset on the experiment, we refer to his optical path design. The pointing jitter noise verification system proposed by CUI et al. [23] in 2022 is regarded as another reference for the following design.

Figure 8 illustrates the experimental setup where a laser undergoes division and frequency alteration through two Acousto-Optic Modulators (AOMs), generating two Gaussian beams with a frequency discrepancy denoted as Δf. In space interference, this

frequency difference is caused by the Doppler frequency shift [6,24]. The Δf is set to 1.6 MHz, which is a value consistent with the Doppler frequency shift of the Taiji program and the detector bandwidth.

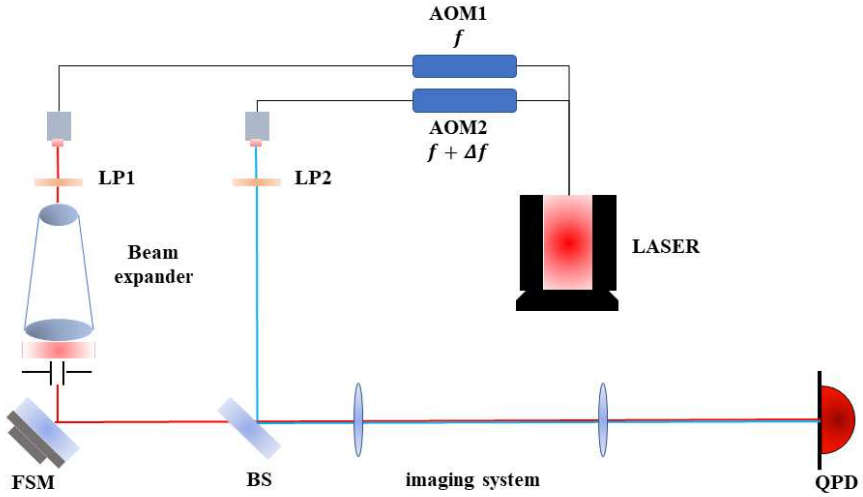

Figure 8. Schematic diagram of the inter-satellite laser link simulation system.

The blue line depicts the reference beam, emulating the local Gaussian beam, which traverses a linear polarizer (LP2) before reflection by a beam splitter (BS). Following this path, the beam navigates through an imaging system and is precisely directed into the QPD's center. During optical path alignment, meticulous care ensures the Gaussian beam's propagation along the optical axis, injecting perpendicularly into the QPD. The QPD's placement on the conjugate plane relative to the waist position aims to negate zero-offset. Conversely, the measurement beam, signified by the red line, proceeds through a distinct linear polarizer (LP1) and a beam expander. This expansion endows the beam with Gaussian flat-top characteristics, mimicking the beam relayed from a distant satellite. A subsequent aperture trims the beam spot to align with the reference spot's dimensions. This beam then reflects off a Fast Steering Mirror (FSM), sequentially moves through BS and the imaging system, and eventually intersects with the reference beam on the QPD, thereby replicating the actual interference conditions of an inter-satellite laser link. In the experiment, optical beam angular deviations induced by pointing jitter are simulated by driving the Fast Steering Mirror (FSM) to generate beam deflections, mimicking the beam walk phenomenon.

To ensure conjugate imaging, the QPD needs to be positioned at the rear focal point of the imaging system, while the FSM should be positioned at the front focal point of the imaging system. To suppress zero-offset and minimize its impact on actual measurements, a reference beam is utilized. By moving the imaging system, a beam quality analyzer is used to find two points with equal beam sizes in the vicinity and far from the rear end of the imaging system. The central position of these two points is considered as the beam waist position. This method effectively locates the beam waist of the reference beam, and iterative adjustments of the imaging system ensure that this point coincides with the rear focal point of the imaging system. The FSM is positioned at the front focal point of the imaging system, which can be determined by the focal length of the lens.

In the Taiji program, the exit pupil position of the measurement beam after four off-axis reflections from the telescope is also the entrance pupil of the optical system. Pointing jitter will couple at this position, affecting interferometric measurements. After completion of the alignment, the entrance pupil position of the optical system is designated as FSM, and using FSM to simulate disturbances aims to achieve results as consistent as possible with actual conditions.

After completing the assembly and alignment of the simulation system, sinusoidal perturbation is applied to FSM in the measurement optical path in the yaw direction to emulate beam walk resulting from pointing jitter inherent in the laser link. This perturbation signal operates at a frequency of 10 mHz, with an amplitude range of 0–800 µrad, under which the DWS angle measurement is assessed. Following this, the imaging system is removed from the optical path, maintaining all other experimental parameters. The DWS angle measurement is then recalculated under this adjusted configuration. This research evaluates the correlation between the beam walk and DWS angle measurement error within the context of an inter-satellite laser link simulation system, focusing on the impact of introducing and subsequently removing the imaging system.

4.2. Results and Discussion

The Figure 9 illustrates the angle measurements depicted by the blue line (without imaging system) and the red line (with imaging system), in contrast to the ideal scenario represented by the gray dotted line, where no measurement error exists. As the perturbation angle expands, there is a corresponding amplification in the measurement inaccuracies relative to the ideal condition. Notably, the error magnitude is considerably more pronounced in the absence of the imaging system. This pattern underscores an escalating nonlinearity in the DWS signal's angle as the beam walk intensifies. Conversely, measurements employing the imaging system more closely mirror the actual perturbation angles, exhibiting enhanced linearity compared to the setup devoid of the imaging system.

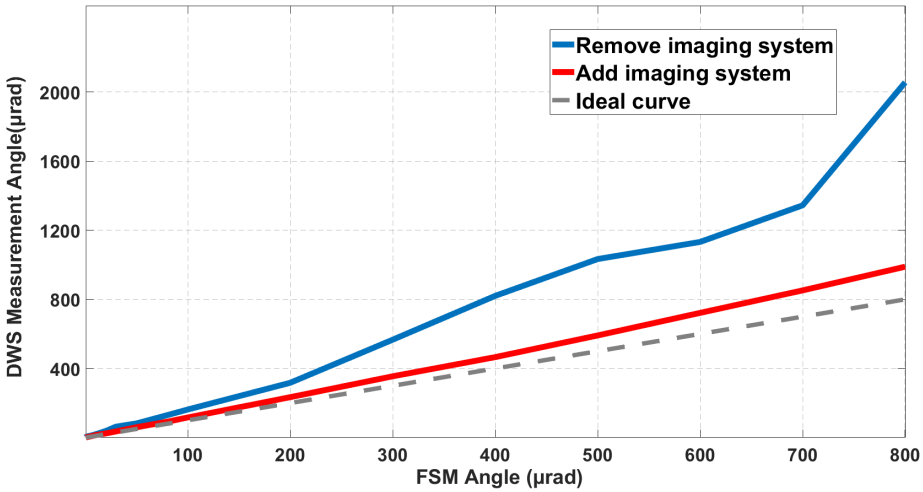

Figure 9. Comparative analysis of the DWS angle measurement error with and without imaging system correction for beam walk.

From the results, it can be observed in Figure 10 that when the piezoelectric-driven amplitude reaches 300 µrad, the addition of the imaging system introduces an angular measurement error of approximately 50 µrad, whereas the error without the imaging system is approximately 300 µrad higher. The inclusion of the imaging system results in a relative reduction in measurement error by 83%. This deviation could potentially stem from optical alignment discrepancies, particularly the misalignment between the two interfering beams or the displacement of the beam center from the QPD's central point. Nonetheless, the integration of the imaging system distinctly amplifies the DWS technique's angle measurement capacity and mitigates measurement inaccuracies. These findings underscore the imaging system's efficacy in rectifying the beam walk.

As shown in Figure 11, when the amplitude applied to the FSM is within 20 µrad, the imaging system still significantly reduces the measurement error of the DWS.

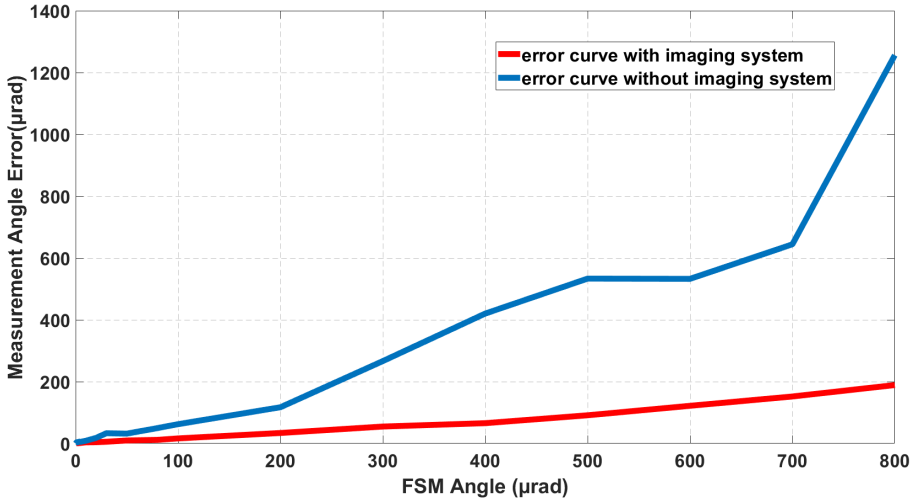

Figure 10. Comparative analysis of angular measurement errors: assessing performance with (red line) and without (blue line) the imaging system.

During ground-based simulations, there is no magnification effect of telescope diagonal jitter. Narrowing the measurement angle range to 20 μrad allows for a clearer assessment of the impact of the imaging system on the precision of QPD capture.

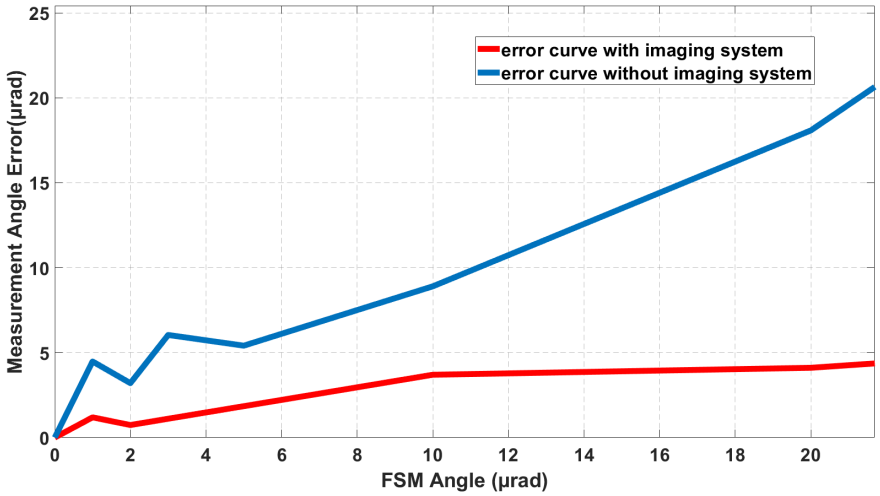

Figure 11. Comparative analysis of angular measurement errors in 20 μrad: assessing performance with (red line) and without (blue line) the imaging system.

For the entire link pointing control system, the stability of the DWS technique in reading out angles also constrains the stability of the link. Therefore, the next step was to test the inhibitory effect of the imaging system on pointing jitter when driving the FSM at different angular offsets.

From Figure 12, it is evident that when the angular deviation of the measurement beam and the reference beam is constant, the root mean square value of jitter measured by the DWS technique is significantly smaller in the optical path with the imaging system compared to when the imaging system is removed. Therefore, the imaging system effectively reduces pointing jitter, and it can be anticipated that further suppression of pointing jitter will occur after closed-loop control by the control system.

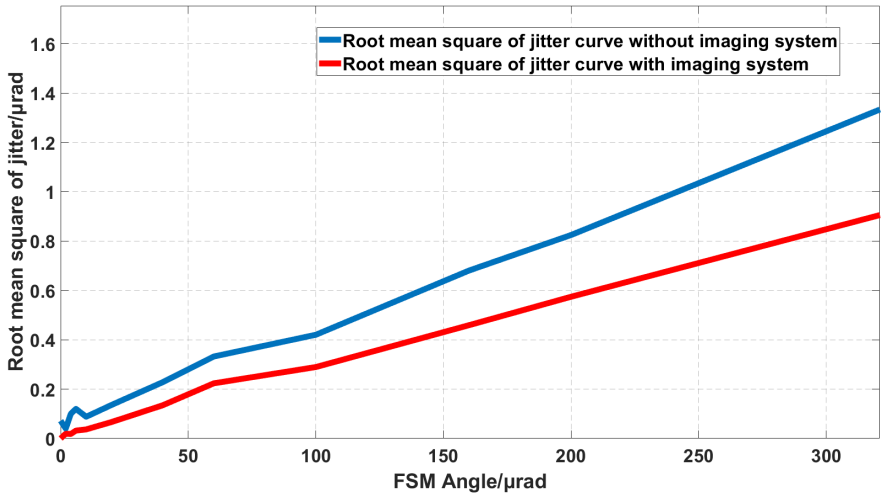

Figure 12. Comparative analysis of jitter RMS: assessing performance with (red line) and without (blue line) the imaging system.

In summary, the integration of the imaging system notably enhances the angular measurement precision and stability of the DWS technique. These results demonstrate the effectiveness of the imaging system in correcting beam wander, making a significant contribution to improving laser pointing accuracy and suppressing inter-satellite link pointing jitter noise.

5. Conclusions

This study explores the complex relationship between the beam walk dimensions and DWS signal in inter-satellite laser communications. Through detailed theoretical analysis and simulations, it becomes evident that an increase in beam walk size leads to heightened nonlinearity in the DWS angle measurements. With a constant pointing jitter, the DWS measurement nonlinear errors caused by different degrees of beam walk will vary with changes in the axial propagation distance, worsening as the degree of beam walk increases. Next, a conjugate imaging system was constructed using two plano-convex lenses to verify the effectiveness of suppressing beam walk through conjugate position imaging. The imaging system can achieve conjugate imaging of the spot centroid within 0.8 mrad with minimal distortion and the introduction of only minor spherical aberration. Then, a ground simulation optical path for DWS angle measurement in inter-satellite links was designed, and the setup and measurements were conducted in the laboratory. By precisely aligning and locating the beam waist and the entrance and exit pupils of the imaging system, alignment errors and the zero-point offset of the DWS technique were suppressed. The experimental results show that with an angular offset of 300 μrad, the measurement error can be reduced to 50 μrad by adding the imaging system to the optical path, which reduces the error by 83% compared to the optical path without the imaging system. When the angular offset is constant, the root mean square value of the QPD measurement jitter is also smaller when the imaging system is added. This indicates that the experimental setup can effectively suppress the nonlinear errors in DWS caused by the beam walk, and the inclusion of the imaging system in the optical path helps to mitigate pointing jitter noise in inter-satellite links, thereby improving laser pointing control accuracy. This method will provide a valuable reference for the QPD interferometric measurement optical path and QPD precision acquisition measurement control on the optical platform in the future Taiji program.

Author Contributions: Conceptualization , X.-G.Q., Y.-K.W. and R.-H.G.; methodology, X.-G.Q. and Z.C.; software, H.-Q.S. and W.-L.Y.; validation, X.-G.Q. and Z.C.; formal analysis, X.-G.Q., X.W., H.-Q.S. and R.-H.G.; investigation, Y.-K.W. and R.-H.G.; resources, Y.-K.W. and R.-H.G.; data curation, X.-G.Q.; writing—original draft preparation, X.-G.Q.; writing—review and editing, X.-G.Q.; visualization, X.-G.Q.; supervision, Y.-K.W.; project administration, Y.-K.W.; funding acquisition, Y.-K.W. All authors have read and agreed to the published version of the manuscript.

Funding: This work was supported by National Key Research and Development Program of China (2022YFC2203700), National Key Research and Development Program of China (2020YFC2201300).

Institutional Review Board Statement: Not applicable.

Informed Consent Statement: Not applicable.

Data Availability Statement: The relevant data and code pertinent to this study are accessible via the provided link (https://pan.baidu.com/s/1FBbJfb92fGTSkfL_3tb6xg) (accessed on 26 May 2023). For access verification codes, please contact qianxingguang21@mails.ucas.ac.cn or the designated corresponding authors' email address. It is advisable to include your affiliation and the purpose of your inquiry in the communication.

Conflicts of Interest: The authors declare no potential conflicts of interest.

References

1. Abbott, B.; Jawahar, S.; Lockerbie, N.; Tokmakov, K. LIGO Scientific Collaboration and Virgo Collaboration (2016) Directly comparing GW150914 with numerical solutions of Einstein's equations for binary black hole coalescence. *Phys. Rev. D* **2016**, *94*, 064035. [CrossRef]
2. Abbott, B.P.; Abbott, R.; Abbott, T.; Abernathy, M.; Acernese, F.; Ackley, K.; Adams, C.; Adams, T.; Addesso, P.; Adhikari, R.X.; et al. Observation of gravitational waves from a binary black hole merger. *Phys. Rev. Lett.* **2016**, *116*, 061102. [CrossRef] [PubMed]
3. Hu, W.R.; Wu, Y.L. The Taiji Program in Space for gravitational wave physics and the nature of gravity. *Natl. Sci. Rev.* **2017**, *4*, 685–686. [CrossRef]
4. Danzmann, K.; Rüdiger, A. LISA technology—concept, status, prospects. *Class. Quantum Gravity* **2003**, *20*, S1. [CrossRef]
5. Danzmann, K.; The LISA Study Team. LISA: Laser interferometer space antenna for gravitational wave measurements. *Class. Quantum Gravity* **1996**, *13*, A247. [CrossRef]
6. Luo, Z.; Guo, Z.; Jin, G.; Wu, Y.; Hu, W. A brief analysis to Taiji: Science and technology. *Results Phys.* **2020**, *16*, 102918. [CrossRef]
7. Luo, J.; Chen, L.S.; Duan, H.Z.; Gong, Y.G.; Hu, S.; Ji, J.; Liu, Q.; Mei, J.; Milyukov, V.; Sazhin, M.; et al. TianQin: A space-borne gravitational wave detector. *Class. Quantum Gravity* **2016**, *33*, 035010. [CrossRef]
8. Crowder, J.; Cornish, N.J. Beyond LISA: Exploring future gravitational wave missions. *Phys. Rev. D* **2005**, *72*, 083005. [CrossRef]
9. Dong, Y.; Liu, H.; Luo, Z.; Li, Y.; Jin, G. Principle demonstration of fine pointing control system for inter-satellite laser communication. *Sci. China Technol. Sci.* **2015**, *58*, 449–453. [CrossRef]
10. Laporte, M.; Halloin, H.; Bréelle, E.; Buy, C.; Grüning, P.; Prat, P. Status of the LISA On table experiment: A electro-optical simulator for LISA. In *Proceedings of the Journal of Physics: Conference Series*; IOP Publishing: Bristol, UK, 2017; Volume 840, p. 012014.
11. Antonucci, F.; Armano, M.; Audley, H.; Auger, G.; Benedetti, M.; Binetruy, P.; Boatella, C.; Bogenstahl, J.; Bortoluzzi, D.; Bosetti, P.; et al. From laboratory experiments to LISA Pathfinder: Achieving LISA geodesic motion. *Class. Quantum Gravity* **2011**, *28*, 094002. [CrossRef]
12. Chwalla, M.; Danzmann, K.; Álvarez, M.D.; Delgado, J.E.; Barranco, G.F.; Fitzsimons, E.; Gerberding, O.; Heinzel, G.; Killow, C.; Lieser, M.; et al. Optical suppression of tilt-to-length coupling in the LISA long-arm interferometer. *Phys. Rev. Appl.* **2020**, *14*, 014030. [CrossRef]
13. Hechenblaikner, G.; Delchambre, S.; Ziegler, T. Optical link acquisition for the LISA mission with in-field pointing architecture. *Opt. Laser Technol.* **2023**, *161*, 109213. [CrossRef]
14. Gao, R.; Liu, H.; Luo, Z.; Jin, G. Introduction of laser pointing scheme in the Taiji program. *Chin. Opt* **2019**, *12*, 425–431.
15. Duan, H.Z.; Liang, Y.R.; Yeh, H.C. Analysis of non-linearity in differential wavefront sensing technique. *Opt. Lett.* **2016**, *41*, 914–917. [CrossRef]
16. Tröbs, M.; Schuster, S.; Lieser, M.; Zwetz, M.; Chwalla, M.; Danzmann, K.; Barránco, G.F.; Fitzsimons, E.; Gerberding, O.; Heinzel, G.; et al. Reducing tilt-to-length coupling for the LISA test mass interferometer. *Class. Quantum Gravity* **2018**, *35*, 105001. [CrossRef]
17. Meshksar, N.; Mehmet, M.; Isleif, K.S.; Heinzel, G. Applying differential wave-front sensing and differential power sensing for simultaneous precise and wide-range test-mass rotation measurements. *Sensors* **2020**, *21*, 164. [CrossRef]
18. Gao, R.; Liu, H.; Luo, Z.; Jin, G. Linearity performance analysis of the differential wavefront sensing for the Taiji programme. *J. Mod. Opt.* **2020**, *67*, 383–393. [CrossRef]

19. Gao, R.; Wang, Y.; Cui, Z.; Liu, H.; Jia, J.; Luo, Z.; Jin, G. Zero-Offset Analysis on Differential Wavefront Sensing Technique in Gravitational Wave Detection Missions. *Microgravity Sci. Technol.* **2023**, *35*, 6. [CrossRef]
20. Wang, S.; Liu, H.; Dai, L.; Luo, Z.; Xu, P.; Li, P.; Gao, R.; Li, D.; Qi, K. Using DWS Optical Readout to Improve the Sensitivity of Torsion Pendulum. *Sensors* **2023**, *23*, 8087. [CrossRef]
21. Xia, Q.; Liang, Y.R.; Yan, H.; Xu, Z.L.; Liu, L.; Zhou, Z.B. High-precision laser beam lateral displacement measurement based on differential wavefront sensing. *Opt. Lett.* **2023**, *48*, 5281–5284. [CrossRef]
22. Yan, H. High-precision comparison method of right dihedral angle using differential wavefront sensing. *Opt. Eng.* **2024**, *63*, 054109. [CrossRef]
23. Cui, Z.; Qian, X.G.; Shi, H.Q.; Ye, Z.J.; Wang, X.; Xing, C.W.; Gao, R.H.; Jia, J.J.; Wang, Y.K.; Wang, J.Y. Research on noise suppression of inter-satellite laser pointing jitter. In Proceedings of the Earth and Space: From Infrared to Terahertz (ESIT 2022), Nantong, China, 17–19 September 2022; SPIE: Bellingham, WA, USA, 2023; Volume 12505, pp. 347–356.
24. Jennrich, O.; Binétruy, P.; Colpi, M.; Danzmann, K.; Jetzer, P.; Lobo, A.; Nelemans, G.; Schutz, B.; Stebbins, R.; Sumner, T.; et al. NGO Assessment Study Report (Yellow Book). 2012. Available online: https://hal.in2p3.fr/hal-00730260/ (accessed on 8 September 2012).